Dynamic Analysis of Multimode Buck–Boost Converter: An LPV System Model Point of View

Jianjun Ma, *Member, IEEE*, Miao Zhu, *Senior Member, IEEE*, Yunwei Li, *Fellow, IEEE*, and Xu Cai

***Abstract*—In dealing with the wide voltage range of energy storage components and fuel cell, multimode buck–boost converter (MBBC) serves as a versatile interfacing circuit with multimode operation capability. In this article, dynamic performance of MBBC is analyzed with consideration of converter operation under multiple modes, and a digital control design method is proposed for fast transient response. The dynamic analysis considers two influence factors, including "transition mode selection" and "close-loop control design." The influences of different Transition mode have been analyzed with the aid of linear parameter varying system, and a new Transition mode has been proposed for the minimum polytopic working region. In "close-loop control design," the recovery time has been minimized with guaranteed robust stability. Compared with small-signal design method, the proposed method not only ensures large-signal stability across multiple working modes, but also offers new insight for Transition mode selection which is overlooked in existing MBBC dynamic analysis. The designed controller has been applied for three representative transition modes, including the first proposed "double-buck-clamping" mode and comparatively evaluated with existing small-signal PI design method.**

***Index Terms*—DC–DC power converters, linear matrix inequity (LMI), large-signal model, multimode control, multimode buck-boost converter.**

I. Introduction

INCREASING applications of energy storage components (battery, supercapacitor, etc.) and fuel cell have been found for electric vehicles [1], [2], distribution system, and dc microgrids [3], [4]. Different from ideal voltage source, the practical output voltage of energy storage component and fuel cell fluctuates with state-of-charge or load condition and varies in wide range. To ensure a stable and regulated output voltage, additional dc–dc converter is often required as the interfacing circuit [5]–[9].

Manuscript received August 12, 2020; revised November 6, 2020; accepted December 15, 2020. Date of publication January 4, 2021; date of current version March 5, 2021. This work was supported in part by the National Key Research and Development Program of China under Grant 2018YFB0904100, and in part by the Science and Technology Project of State Grid under Grant SGHB0000KXJS1800685. Recommended for publication by Associate Editor L. Corradini. *(Corresponding author: Miao Zhu.)*

Jianjun Ma, Miao Zhu, and Xu Cai are with the School of Electronic Information and Electrical Engineering, Shanghai Jiao Tong University, Shanghai 200240, China, and also with the Key Laboratory of Control of Power Transmission and Conversion, Ministry of Education, Shanghai 200240, China (e-mail: j.j.ma@sjtu.edu.cn; miaozhu@sjtu.edu.cn; xucai@sjtu.edu.cn).

Yunwei Li is with the Department of Electrical and Computer Engineering, University of Alberta, Edmonton, AB T6G 2V4, Canada (e-mail: yunwei.li@ualberta.ca).

Color versions of one or more figures in this article are available at https://doi.org/10.1109/TPEL.2020.3048775.

Digital Object Identifier 10.1109/TPEL.2020.3048775

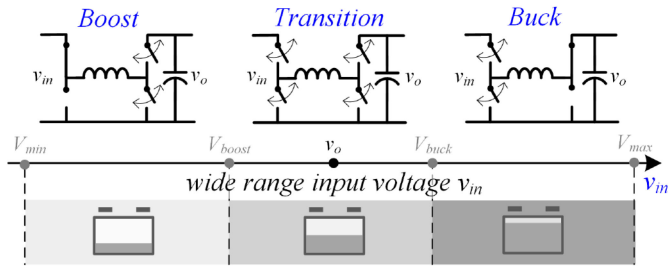

Fig. 1. Multimode operation of MBBC under wide-range input voltage $v_{\rm in}$.

As shown in Fig. 1, multimode buck–boost converter (MBBC) can be flexibly configured in *buck* mode or *boost* mode and have wide voltage conversion capability. During these two modes, only two power switches operate during each cycle and high converter efficiency can thus be maintained through a wide operation range [10]–[12]. Due to the advantages of multimode operation, MBBC has been adopted for many applications, such as automotive electric system [1], [2], [6], [7] and distributed generation system [3], [13], [14]. The converter has also been named as boost+buck converter [1], positive buck–boost converter [15], noninverting buck–boost converter [16], etc.

However, multimode operation inherently brings new challenges to open-loop dynamic analysis and close-loop control design. Due to the presence of switch dead-time and control delay, there is a gap of voltage conversion ratio between *buck* and *boost* mode [15]–[20]. To eliminate the discontinuity, an additional *Transition* mode is required between them, as shown in Fig. 1. The real-time working mode can be determined by comparing the input voltage $v_{\rm in}$ with the output voltage v_o. When $v_{\rm in}$ is higher than v_o, MBBC works in *buck* mode. When $v_{\rm in}$ is lower than v_o, MBBC works in *boost* mode. When $v_{\rm in}$ and v_o are near, MBBC works in *Transition* mode.

A. Researches on Transition Mode

Existing research on the *Transition* mode mainly concerns with the converter efficiency. For optimization of the efficiency, a series of *Transition* mode has been proposed, from the one-section *Transition* mode such as "*buck–boost*" mode [10], "*boost-clamping*" mode [21], to two-section *Transition* mode such as "*extend-buck+extend-boost*" mode [11] and to the N-section *Transition* mode [18].

Apart from steady-state efficiency, the different *Transition* modes are expected to present different dynamic properties. The lingering question is "How to evaluate the influence of

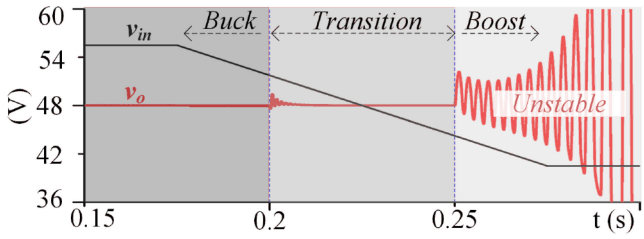

Fig. 2. PI control stable for "*Buck* mode" and "*Transition* mode" leads to instability in "*Boost* mode."

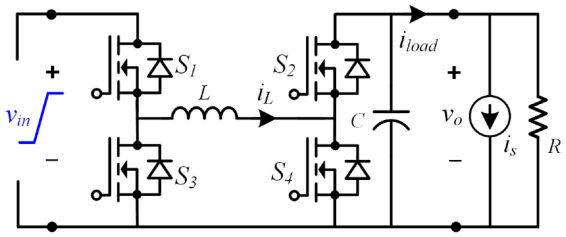

Fig. 3. Circuit diagram of MBBC for output voltage v_o regulation.

different *Transition* modes on MBBC dynamic performance?" Answer to the question will be the key for transient performance optimization. To the best of our knowledge, no existing literature has covered this issue. The probable reason may due to the lack of modeling and control technique applicable for multimode converter.

B. Researches on Control Design

Small-signal method is the mostly applied converter modeling technique [5]. The nonlinear power converter is modeled as a linear system at the corresponding steady-state working point. For the case of MBBC, the main problem is to select the appropriate steady-state point that mostly represents the converter properties in all three modes [21]–[26]. An example of PI control designed on the small-signal model is shown in Fig. 2. In the design case, the small-signal model is developed at *buck* mode. The designed PI controller also performs well in *Transition* mode. However, as soon as the converter enters *boost* mode, the output voltage v_o becomes unstable. A further analysis on the problems of small-signal model based control design is given in Section II.

Apart from the small-signal method, some large-signal control has also been proposed. The circular switching surface has been applied for stabilization of MBBC interfaced with constant power load in [2]. In [27], trajectory control has been adopted for fast transient process, and the implementation would require accurate circuit parameters and high-precision sensors. Sliding mode control has been investigated in [28], [29] for robust voltage regulation. As for dynamic performance optimization, the linear matrix inequity (LMI) proves to be an efficient method to deal with the wide-range operation of boost converter and varying grid frequency of inverter [30], [31]. The potential application of LMI method for multimode MBBC still remains unexplored.

With consideration of MBBC dynamic differences under multiple working modes, a linear control design algorithm is proposed in this article for both robust stability and fast transient performance. Operation of MBBC and the potential instability of small-signal design method are first analyzed in Section II. Instead of small-signal model, MBBC is first modeled as linear parameter varying (LPV) system with 3-D working region. The influences of different *Transition* modes can thus be evaluated based on the size of the region. A novel *Transition* mode "*Double-buck-clamping*" is first proposed for the optimal open-loop dynamic in Section III. The classical control structure is preserved and the control gains are optimized through LMI method in Section IV. The proposed control is compared with small-signal PI control in Section V. Besides, the proposed *Transition* mode and close-loop control are also comparatively validated through experimental results in Section V.

II. Review on Multimode Operation of MBBC

The MBBC power circuit is shown in Fig. 3, and the norton-equivalent circuit of converter load is given as a resistor R in parallel with a current source i_s. During normal operation, S_1 (S_2) works in complement with S_3 (S_4). The total load current is represented by i_{load}.

The average model of MBBC circuit in Fig. 3 is given as (1), where v_{in} is the input voltage, v_o is the output voltage, i_L is the inductor current, d_1 and d_4 denote the duty ratio of power switch S_1 and S_4, respectively. Under continuous current mode operation, the equivalent on-time ratio of power switch S_2 is defined as d_2:

$$\begin{cases} L\frac{di_L(t)}{dt} = d_1(t)\, v_{\text{in}}(t) - [1 - d_4(t)]\, v_o(t) \\ C\frac{dv_o(t)}{dt} = [1 - d_4(t)]\, i_L(t) - \frac{v_o(t)}{R} - i_s(t) \end{cases} \tag{1}$$

$$d_2(t) = 1 - d_4(t). \tag{2}$$

During steady-state, the voltage conversion ratio K is given by (3), where D_1 and D_2 are the steady-state duty cycle of S_1 and S_2, respectively,

$$K = \frac{V_o}{V_{\text{in}}} = \frac{D_1}{D_2}. \tag{3}$$

A. Steady-State Operation

If take D_1 as the vertical axis and D_2 as the lateral axis, a graphic representation of K is the slope of line connecting "O" and the working point (D_1, D_2), as illustrated in Fig. 4. In "*buck* mode", S_2 is constantly closed ($D_2 = 1$) and the working area is B_1B_2. In "*boost* mode", S_1 is constantly closed ($D_1 = 1$) and the working area is A_1A_2. Due to the presence of switch dead time and control delay, both D_1 and D_2 have the maximum value $D_{\max}$. It will lead to a discontinuous voltage conversion ratio between OA_1 ($K = 1/D_{\max}$) and OB_1 ($K = D_{\max}$), as shown in Fig. 4. To ensure a continuous voltage conversion, MBBC has to operate within the area σ, and the working mode is named as "*Transition* mode."

Within σ, any line connecting C_1C_2 with E_1E_2 can be adopted as the *Transition* mode, as represented by C_kE_k in Fig. 4. The *Transition* mode can be one section such as *boost-clamping*

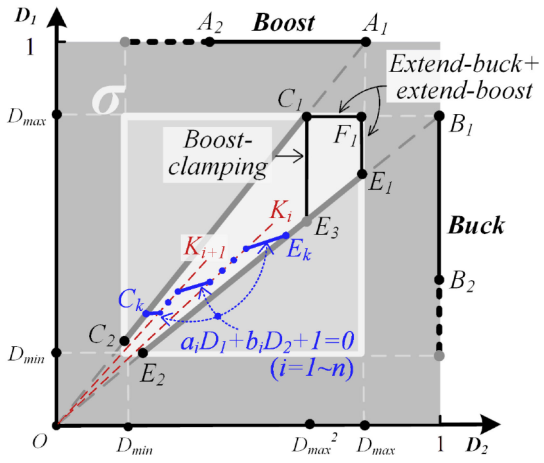

Fig. 4. Illustration of MBBC working modes in (D_1, D_2) plane.

mode [21], or consist of two sections such as "*extend-buck+extend-boost*" mode [11].

A general representation for the *Transition* mode that consists of n piecewise sections is given by (4), where a_i and b_i are coefficients relating to the ith ($i = 1\sim n$) section *Transition* mode, K_i ($i = 1\sim n$) corresponds to the voltage conversion ratio at the ith section.

$$\begin{aligned} &a_iD_1 + b_iD_2 + 1 = 0\ ,\ V_o/V_{\text{in}} \in [K_i, K_{i+1}] \\ &(i = 1 \sim n,\ D_{\max} \le K_i < K_{i+1} \le 1/D_{\max})\,. \end{aligned} \tag{4}$$

For example, if the *Transition* mode is *boost-clamping* mode, $n = 1$ with $a_1 = 0, b_1 = -1/{D_{\max}}^2$. If the *Transition* mode is *buck–boost* mode, $n = 1$ with $a_1 = -1, b_1 = -1$. If the *Transition* mode is *extend-buck+extend-boost* mode, $n = 2$ with $a_1 = 0$, $b_1 = -1/D_{\max}$, $a_2 = -1/D_{\max}$, $b_2 = 0$.

B. Problems of Small-Signal Model Based Control Design

For control design of MBBC, the small-signal model can be derived by first linearize and discretize the average model of (1) at the corresponding working point (I_L, D_1, D_2, V_{in}, V_o). The discrete-time representation of MBBC is given by (5), where the upper-case letter denotes the dc value, and the lowercase letter with hat ($\sim$) denotes the perturbation term. The sampling period is given by T_s [32].

$$\begin{cases} \tilde{i}_L(k+1) = \tilde{i}_L(k) - \frac{D_2T_s}{L}\tilde{v}_o(k) + \frac{V_{\text{in}}T_s}{L}\tilde{d}_1(k) \\ \qquad\qquad + \frac{V_oT_s}{L}\tilde{d}_4(k) + \frac{D_1T_s}{L}\tilde{v}_{\text{in}}(k) \\ \tilde{v}_o(k+1) = \frac{D_2T_s}{C}\tilde{i}_L(k) + \left(1 - \frac{T_s}{RC}\right)\tilde{v}_o(k) \\ \qquad\qquad - \frac{I_LT_s}{C}\tilde{d}_4(k) - \frac{T_s}{C}\tilde{i}_s(k)\,. \end{cases} \tag{5}$$

During each mode, the two control variables d_1, d_4 in (5) are interdependent and a unified duty ratio d can be adopted for all three working modes.

1) In *buck* mode, d_4 is a constant value of 0 and d_1 is the active duty ratio d.

$$\textbf{Buck}:\ \tilde{d}_1(k) = \tilde{d}(k)\,,\ \tilde{d}_4(k) = 0. \tag{6}$$

TABLE I
PARAMETERS OF MBBC CONVERTER

Parameter	Value	Nominal Value
L	0.4mH	–
C	330μF	–
R	40Ω	–
I_s	[0,4] A	2A
D_{max}	0.9	–
Switching frequency f_s	20kHz	–
V_o	48 V	–
V_{in}	*Boost*: [24,44] *Transition*: [44,53] *Buck*: [53,72]	*Boost*: 34V *Transition*:48V *Buck*: 63V

2) In *boost* mode, d_1 is a constant value of 1 and d_4 is the active duty ratio d.

$$\textbf{Boost}:\ \tilde{d}_1(k) = 0,\ \tilde{d}_4(k) = \tilde{d}(k)\,. \tag{7}$$

3) In *Transition* mode, the active duty ratio relates with the corresponding *Transition* mode parameters a_i, b_i in (4). If $a_i = 0$, d_4 is a constant value and d_1 is the active duty ratio d. If $a_i \neq 0$, d_4 is the active duty ratio d. Relationship of the perturbation of d_1 and d_4 is given by (8).

$$\textbf{Transition}:\begin{cases} (a_i = 0):\ \tilde{d}_1(k) = \tilde{d}(k)\,,\ \tilde{d}_4(k) = 0 \\ (a_i \neq 0):\ \tilde{d}_1(k) = \frac{b_i}{a_i}\tilde{d}(k)\ \tilde{d}_4(k) = \tilde{d}(k)\,. \end{cases} \tag{8}$$

Based on (5)–(8), the small-signal model of MBBC can be derived after selecting the working point (I_L, D_1, D_2, V_{in}, V_o). For the considered operation case listed in Table I, the open-loop $v_o\sim d$ frequency response is shown in Fig. 5. It varies in wide range depending on the operation condition. For small-signal control design, the main problems come in two aspects as follows:

1) Small-signal model only reflects the dynamic property near the selected operation point. As a result, stability of the designed control can only be assured at the selected working mode and operation point. For example, if the operation point is selected at *buck* mode, the designed controller ***PI* 1** (voltage-loop $k_p = 0.44$, $k_i = 6770$, current loop $k_p = 0.06$, $k_i = 827$) can ensure stable operation, as the operation point ***A*** in Fig. 5. However, under the same controller, the converter will become unstable in *boost* mode, as indicated by the operation point ***C***. The reason is that *boost* mode has a RHP zero and leads to lower phase margin.

To account for the influence of RHP zero, [22], [23] have proposed to select the steady-state point at *boost* mode. However, the RHP zero may also appear at *Transition* mode, as in [10], [11]. If the PI control design based on small-signal model in *boost* mode, as the controller ***PI* 2** (voltage-loop $k_p = 1.76$, $k_i = 5082$, current loop $k_p = 0.33$, $k_i = 827$), the controller can ensure enough phase margin at *boost* mode, as the operation point ***B*** in Fig. 5. However, the converter becomes unstable at the *Transition* mode ($a_1 = -1, b_1 = -1$), as the operation point ***D***. It is theoretically possible to check all steady-state operation points,

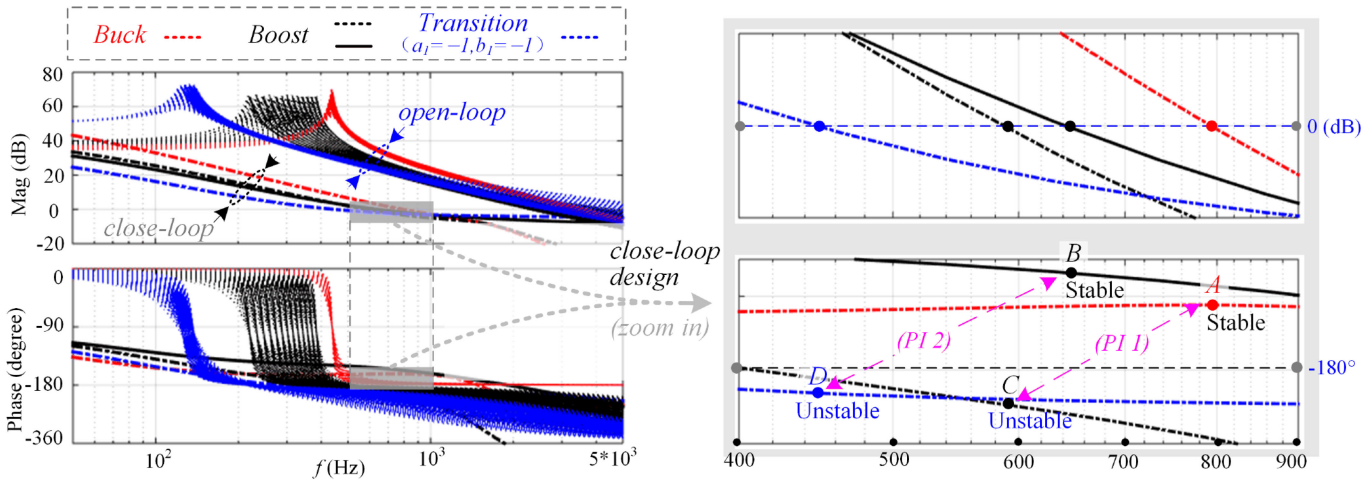

Fig. 5. v_o∼d frequency response of multimode buck–boost converter in open-loop and close-loop control.

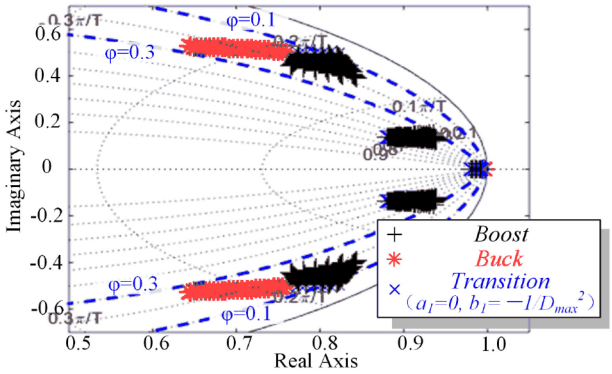

Fig. 6. Close-loop eigenvalues of MBBC with small-signal model based PI control design.

however, this trial-and-error process will be time-consuming and inefficient.

2) Small-signal model based design only provide control optimization near the operation point, and unable for dynamic optimization at the wide working region.

For example, based on the small-signal model in *buck* mode with $V_{\text{in}} = 24$ V, and $I_s = 0$ A. The current loop is designed with crossover frequency at $f_s/10$ with phase margin of 45°, the voltage loop is designed with 1/5 current-loop crossover frequency with phase margin of 50°. The designed ***PI*** control parameters are voltage-loop $k_p = 1.3$, $k_i = 4630$, current loop $k_p = 0.06$, and $k_i = 1070$. Based on digital implementation, the close-loop eigenvalues of MBBC under the whole working range is shown in Fig. 6.

During *buck* mode, the damping ratio of the designed control can reach 0.3. However, for operation point in *boost* mode, the damping ratio of designed control can be below 0.1 and results in poor dynamic performance. A further experimental verification of small-signal model based control design is given in Section V.

In summary, the small-signal model only provides limited information at the selected steady-state point and working mode. Stability and dynamic responses of the designed controller would not be guaranteed in the other working modes. Therefore large-signal performance of MBBC should be considered collectively during modeling as well as control design stage.

III. Open-Loop Dynamics of MBBC

For analysis of MBBC dynamics under multimode operation, the converter is considered as an LPV system. Different from small-signal model, the dc values (D_1, D_2, V_{in}, V_o, I_L) are deemed as varying terms relating to the working mode and operation condition.

A. LPV System Model

In (5), i_L and v_o are internal state variables of MBBC. i_s and v_{in} are external variables relating to load condition and input voltage, respectively. For battery and fuel cell, fluctuations of v_{in} generally appear at low-frequency level below 200 Hz [35], [36]. To focus on MBBC dynamic performance of load response, the primary disturbance term is taken as the load disturbance i_s, and input voltage variation is deemed as negligible. For cases when the disturbance of v_{in} cannot be neglected, it can be compensated through feed-forward method in [23] and the work is not repeated here. As a result, only load disturbance i_s is considered in the following.

Besides, considering the inherent one duty cycle control delay of digital implementation, an intermediate variable $u[k]$ is introduced as follows:

$$\tilde{u}(k) = \tilde{d}(k+1). \tag{9}$$

By combining (5)–(9) and neglecting the input voltage variation, the discrete-time MBBC model can be unitedly represented as (10).

The varying parameters can be categorized into two types: 1) Parameters relating to input/output voltage status, including λ_1, λ_2, and λ_3. 2) Parameters relating to load status, including R and the total load current I_{load}. When the output voltage V_o is regulated at the reference value, R and I_{load} are solely determined by the external load. Therefore, the key of dynamic performance

optimization lies in λ_1, λ_2, and λ_3

$$\begin{bmatrix} \tilde{i}_L(k+1) \\ \tilde{v}_o(k+1) \\ \tilde{d}(k+1) \end{bmatrix} = \underbrace{\begin{bmatrix} 1 & -\frac{T_s}{L}\lambda_1 & \frac{V_o T_s}{L}\lambda_3 \\ \frac{T_s}{C}\lambda_1 & 1-\frac{T_s}{RC} & -\frac{I_{\text{load}} T_s}{C}\lambda_2 \\ 0 & 0 & 0 \end{bmatrix}}_{A(\lambda)} \begin{bmatrix} \tilde{i}_L(k) \\ \tilde{v}_o(k) \\ \tilde{d}(k) \end{bmatrix} + \underbrace{\begin{bmatrix} 0 \\ 0 \\ 1 \end{bmatrix}}_{B_u} \tilde{u}(k) + \underbrace{\begin{bmatrix} 0 \\ -\frac{T_s}{C} \\ 0 \end{bmatrix}}_{B_{is}} \tilde{i}_s(k). \quad (10)$$

In each mode, the corresponding values of λ_1, λ_2, and λ_3 are summarized in (11). According to (11), the MBBC model varies with working mode and operating condition (D_1, D_2, V_{in}, V_o). These varying parameters formed a polytopic working region in the 3-D space (λ_1, λ_2, λ_3).

$$\lambda_1 = D_2$$

$$\lambda_2 = \begin{cases} 0 & (Buck) \\ 0 & (Transition,\ a_i = 0) \\ \frac{1}{D_2} & (Transition,\ a_i \neq 0) \\ \frac{1}{D_2} & (Boost) \end{cases}$$

$$\lambda_3 = \begin{cases} \frac{V_{\text{in}}}{V_o} & (Buck) \\ \frac{V_{in}}{V_o} & (Transition,\ a_i = 0) \\ \frac{b_i}{a_i}\frac{V_{\text{in}}}{V_o} + 1 & (Transition,\ a_i \neq 0) \\ 1 & (Boost). \end{cases} \quad (11)$$

According to convex theory, size of the polytopic region is closely related with the converter control performance, which has been described by the so-called "vertex property" of convex set [33], [34]: *For LPV system, the larger polytopic working region is, the more conservative LMI synthesized results will be*.

As a result, optimization of open-loop dynamics of MBBC is attributed to minimization of the convex region formed by the varying parameters λ_1, λ_2, and λ_3.

B. Minimization of (λ_1, λ_2) Polygon Region

First consider the varying parameters λ_1 and λ_2. In the 2-D (λ_1, λ_2) plane, the convex set refers to the polygon that covers working region in all three working modes. Based on (11), the relationship between working mode in (D_1, D_2) plane and region in (λ_1, λ_2) plane are shown in Fig. 7(a) and (b), respectively. The aim of this section is to find the *Transition* mode that has the minimum polygon in (λ_1, λ_2) plane.

1) In *buck* mode, the working mode B_1B_2 in Fig. 7(a) is mapped to the point B_1 (1, 0) in Fig. 7(b).
2) In *boost* mode, the working mode A_1A_2 (or A_1A_3) in Fig. 7(a) is mapped to the arc A_1A_2 (or A_1A_3) in Fig. 7(b). According to (11), the arc locates on the curve of $\lambda_2 = 1/\lambda_1$. One of the terminal A_1 is fixed at ($D_{\max}$, $1/D_{\max}$). The other terminal fluctuates with the minimum input voltage, and can be A_2 or A_3.
3) In *Transition* mode, according to (11), the (λ_1, λ_2) operation region relates with parameter a_i ($i = 1 \sim n$) value at the ith section. When $a_i \neq 0$, by combining (2)–(3) with (11), the ith *Transition* mode region $C_1F_kE_k$ also locates on the curve $\lambda_2 = 1/\lambda_1$ in Fig. 7(b). When $a_i = 0$, the ith *Transition* mode region locates on the λ_1 axis and is represented by the point F in Fig. 7(b).

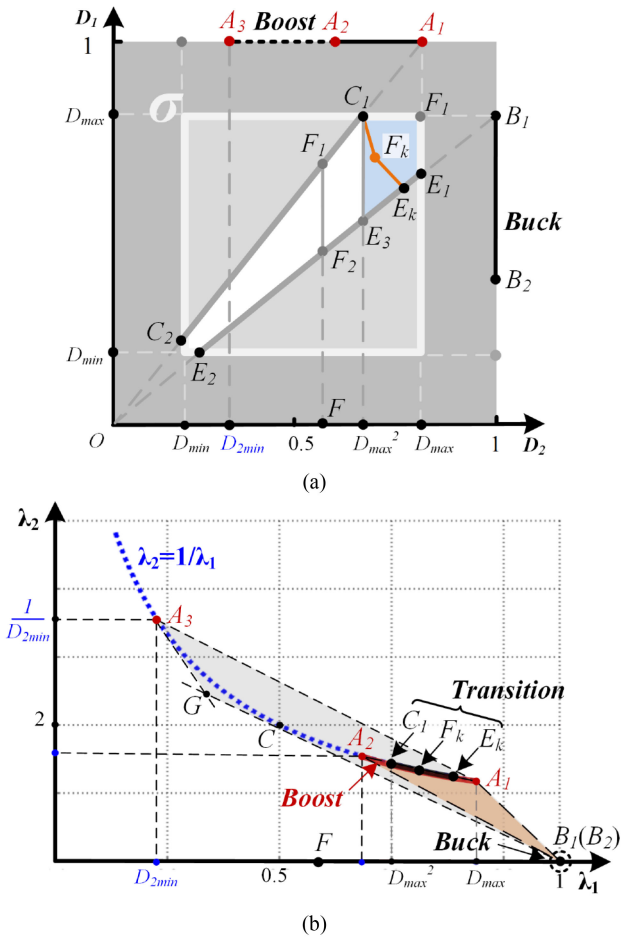

Fig. 7. Relationship between MBBC working mode in (D_1, D_2) plane and polygon regions in (λ_1, λ_2) plane when the maximum V_o/V_{in} is above $1/D_{\max}^2$. (a) Working mode in (D_1, D_2) plane. (b) Polygon regions in (λ_1, λ_2) plane.

The value range of D_2 at the ith *Transition* mode can be developed by combing (2)–(4) as (12)

$$D_2 \in \left[\frac{-1}{a_iK_i + b_i}, \frac{-1}{a_iK_{i+1} + b_i}\right],\ a_i \geq 0$$
$$\text{or } \left[\frac{-1}{a_iK_{i+1} + b_i}, \frac{-1}{a_iK_i + b_i}\right],\ a_i < 0. \quad (12)$$

With consideration of all three working modes, the general polygon in (λ_1, λ_2) plane is represented by $\boldsymbol{P}(\lambda_1, \lambda_2)$.

$$\boldsymbol{P}(\lambda_1, \lambda_2) = \text{Convex}\left\{\underbrace{B_1}_{Buck}, \underbrace{A_1A_2}_{Boost}, \underbrace{C_1F_kE_k \text{ or } F}_{Transition}\right\}. \quad (13)$$

For applications with the maximum voltage conversion ratio $V_o/V_{\min} > 1/D_{\max}^2$, the operation point A_2 in *boost* mode locates on the left side of $\lambda_1 = D_{\max}^2$, as shown in Fig. 7(a)

If the *Transition* mode locates inside the trapezoid $C_1F_1E_1E_3$ in Fig. 7(a) with $a_i \neq 0$ ($i = 1 \sim n$), the corresponding region $C_1F_kE_k$ in Fig. 7(b) will locate within the A_1A_2. This relationship is represented by $C_1F_kE_k \subseteq A_1A_2$. As a result, the total polygon $\boldsymbol{P}(\lambda_1, \lambda_2)$ of (13) can be developed as $\boldsymbol{P}_{C1F1E1E3}(\lambda_1, \lambda_2)$ as follows:

$$\boldsymbol{P}_{C1F1E1E3}(\lambda_1, \lambda_2) = \text{Convex}\left\{\underbrace{B_1}_{Buck}, \underbrace{A_1A_2}_{Boost}\right\}. \quad (14)$$

The polygon $\boldsymbol{P}_{C1F1E1E3}(\lambda_1, \lambda_2)$ in (14) is irrelevant with *Transition* mode, and $\boldsymbol{P}_{C1F1E1E3}(\lambda_1, \lambda_2) \subseteq \boldsymbol{P}(\lambda_1, \lambda_2)$ always hold. In comparison, if any of the *Transition* mode section appears with $a_i = 0$ ($i = 1 \sim n$), or locates outside the trapezoid $C_1F_1E_1E_3$ in Fig. 7(a), $C_1F_kE_k \subseteq A_1A_2$ will no longer hold. Therefore, $\boldsymbol{P}_{C1F1E1E3}(\lambda_1, \lambda_2)$ in (14) is the minimum polygon.

Construction of the polygon $\boldsymbol{P}_{C1F1E1E3}(\lambda_1, \lambda_2)$ involves with the maximum voltage conversion ratio in *boost* mode. As shown in Fig. 7(b), if the maximum voltage conversion ratio is lower than 2, the corresponding *boost* mode operation region locates at the right side of C (0.5, 2), such as the arc A_1A_2, and the polygon is the triangle $A_1B_1A_2$. If the maximum voltage conversion ratio is higher than 2, the corresponding *boost* mode operation region will appear at the left side of C (0.5, 2), such as the arc A_1A_3 in Fig. 7(b). The polygon can be formed by the line A_3G, A_3A_1, A_1B_1, and GB_1. Assuming the minimum value of D_2 at *boost* mode is $D_{2\min}$, the equations of A_3G, GB_1 and their crossover point G are given as follows:

$$\begin{cases} GB_1 : 4\lambda_1 + \lambda_2 = 4 \\ A_3G : \lambda_1 + (D_{2\min})^2\lambda_2 = 2D_{2\min} \end{cases} \quad (15)$$

$$G : \left(\frac{2D_{2\min} - 4D_{2\min}^2}{1 - 4D_{2\min}^2}, \frac{4 - 8D_{2\min}}{1 - 4D_{2\min}^2}\right). \quad (16)$$

In summary, to attain the minimum polygon in (λ_1, λ_2) plane, the feasible Transition mode is restricted within $C_1F_1E_1E_3$ in Fig. 7(a). The above conclusion applies for the maximum voltage conversion ratio is larger than $1/D_{\max}{}^2$. For typical $D_{\max} > 0.9$, it requires the maximum voltage conversion ratio higher than 1.2. This condition can be easily met for practical applications of MBBC, as in [6]–[16].

For a complete analysis, cases for the maximum voltage conversion ratio below $1/D_{\max}{}^2$ are also analyzed in the following. It should be noted that the majority of applications belongs to the previous scenario with $V_o/V_{\min} > 1/D_{\max}{}^2$.

For the *Transition* mode consists of n piecewise sections given by (4), consider the last nth section in connection with C_1C_2. If $a_n \neq 0$, such as C_kF_{nk} in Fig. 8(a), the operation region is mapped to C_kF_{nk} in Fig. 8(b) and locates on the curve $\lambda_2 = 1/\lambda_1$. Construction of the polygon follows the same method in Fig. 7(b). To search for the minimum polygon, C_k can moves on C_1C_2 in Fig. 8(a). The corresponding operation region moves on the curve $\lambda_2 = 1/\lambda_1$ in Fig. 8(b). The minimum polygon $A_1B_1C_1$ is reached with C_k moves to C_1. Besides, for the rest of the $n-1$ sections of *Transition* modes, if $a_i = 0$ ($i = 1 \sim n-1$), the corresponding working point appears at the λ_1 axis and results in larger polygon. Therefore, when $a_n \neq 0$, all the n sections of

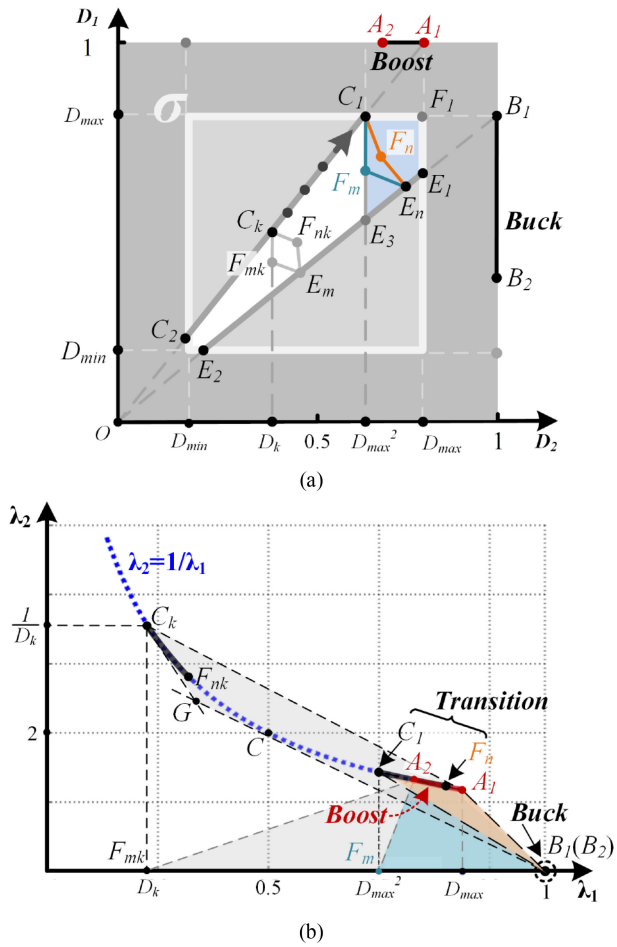

Fig. 8. Relationship between MBBC working mode in (D_1, D_2) plane and polygon regions in (λ_1, λ_2) plane when the maximum V_o/V_{in} is below $1/D_{\max}{}^2$. (a) Working mode in (D_1, D_2) plane. (b) Polygon regions in (λ_1, λ_2) plane.

Transition mode should locate inside $C_1F_1E_1E_3$ in Fig. 8(a) with $a_i \neq 0$ ($i = 1 \sim n$).

If $a_n = 0$, such as C_kF_{mk} in Fig. 8(a), the operation region locates on the λ_1 axis in Fig. 8(b). To search for the minimum polygon, C_k can moves on C_1C_2 in Fig. 8(a). The corresponding operation point F_{mk} moves on the λ_1 axis in Fig. 8(b). The minimum polygon $A_2A_1B_1F_m$ is reached when F_{mk} moves to F_m. Besides, for the n piecewise *Transition* mode, if $a_i \neq 0$ ($i = 1 \sim n-1$) appears, the corresponding *Transition* mode region will appear on the curve $\lambda_2 = 1/\lambda_1$ and leads to larger polygon. Therefore, when $a_n = 0$, $a_i = 0$ ($i = 1 \sim n-1$) should also holds for rest of the $n-1$ sections. The resulting *Transition* mode is C_1E_3 in Fig. 8(a) and is also known as *boost-clamping* mode. In summary, for the two cases of $a_n \neq 0$ and $a_n = 0$, the corresponding two minimum polytopic working regions are the triangle $A_1B_1C_1$ and the trapezoid $A_2A_1B_1F_m$ in Fig. 8(b), respectively. There is no inclusion relationship between the two regions. As a result, both the two candidate *Transition* modes should be checked during close-loop control design.

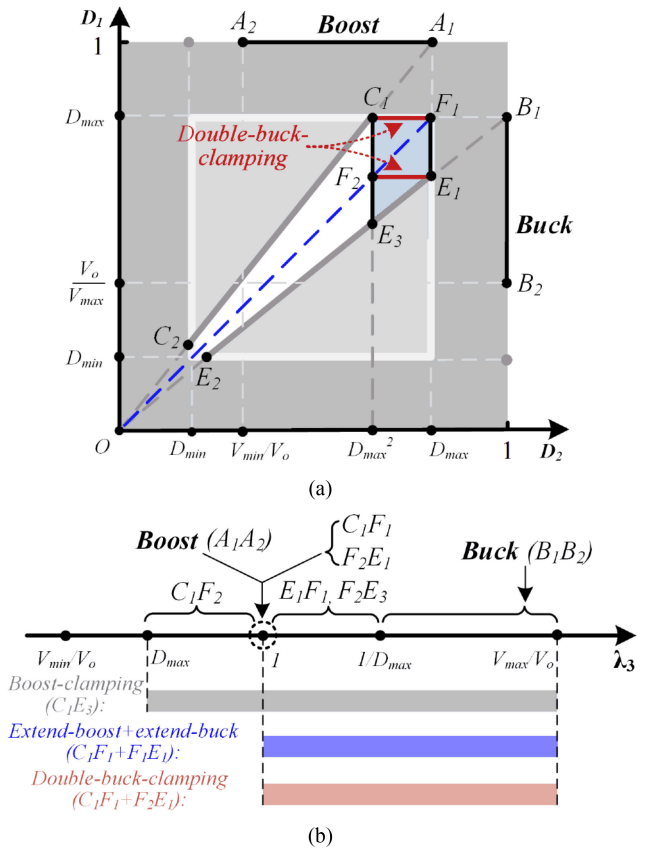

Fig. 9. Relationship between MBBC working region and λ_3 varying ranges. (a) MBBC working mode in (D_1, D_2) plane. (b) λ_3 varying ranges.

From the above analysis, to attain the minimum polygon in (λ_1, λ_2) plane, the feasible *Transition* mode is restricted inside $C_1F_1E_1E_3$ in (D_1, D_2) plane.

C. Minimization of (λ_1, λ_2, λ_3) Polytope Region

Based on the above discussion in (λ_1, λ_2) plane, the additional varying parameter λ_3 is included for minimization of the polytope in 3-D (λ_1, λ_2, λ_3) space. Different from λ_1, λ_2, the varying parameter λ_3 is determined by voltage conversion ratio and *Transition* mode parameters a_i, b_i. The relationship of working mode in (D_1, D_2) plane and λ_3 varying range is shown in Fig. 9.

1) In *buck* mode, λ_3 is determined by the voltage conversion ratio and varies in $[1/D_{\max}, V_{\max}/V_o]$.
2) In *boost* mode, λ_3 is rigid as 1.
3) In *Transition* mode, the varying range relates with a_i value at the ith ($i = 1 \sim n$) *Transition* mode. According to the above analysis, to attain the minimum polygon in (λ_1, λ_2) plane, the *Transition* mode should be confined within the trapezoid $C_1F_1E_1E_3$.

As for the varying range of λ_3, it is related with slope of the *Transition* mode b_i/a_i. If $b_i = 0$, λ_3 is rigid as 1 according to (12) and overlaps with *boost* mode. As a result, λ_3 reaches the minimum varying range of $[1, V_{\max}/V_o]$ as in Fig. 9(b). Since the *Transition* mode should also be confined within the trapezoid

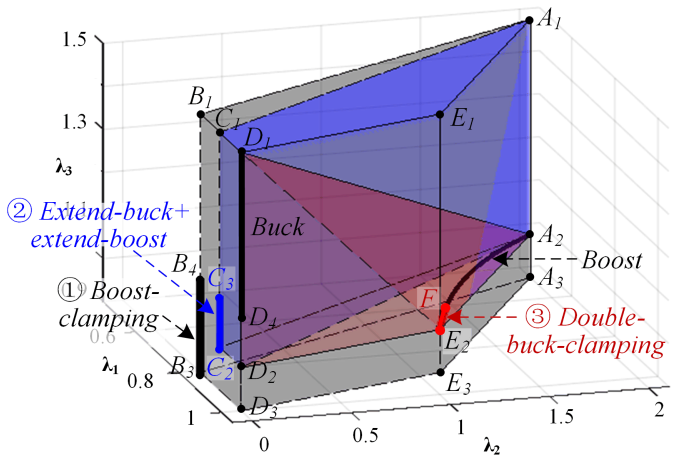

Fig. 10. Comparison of MBBC polytopes in three-dimensional (λ_1, λ_2, λ_3) space with different *Transition* modes.

$C_1F_1E_1E_3$. The corresponding *Transition* mode would consists of two parts of "F_2E_1+C_1F_1" as shown in Fig. 9(a). This novel *Transition* mode is proposed as "*Double-buck-clamping*" mode.

Based on the above analysis, the polytope in (λ_1, λ_2, λ_3) space can be formed by the polygon in (λ_1, λ_2) plane and the varying range of λ_3. With the case in Table I, a comparison of the polytope in (λ_1, λ_2, λ_3) space is shown in Fig. 10.

For *buck* mode, the corresponding region is the line D_1D_4. For *boost* mode, the corresponding region is the arc E_2A_2. If the *Transition* mode is selected as *double-buck-clamping*, the *Transition* mode region is the arc E_2F and locates within the arc E_2A_2. The total polytope is only determined by *buck* mode and *boost* mode. Note that *buck* mode region D_1D_4 is vertical to (λ_1, λ_2) plane, the polytopic working region is given by the tetrahedron $D_1D_2E_2A_2$ in Fig. 10.

In comparison, if the *Transition* mode is selected as *boost-clamping* mode, the operation region is B_4B_3. If the *Transition* mode is selected as *extend-buck*+*extend-boost* mode, the operation region is C_3C_2. Both of the two *Transition* mode regions locate outside *buck* and *boost* mode region, and lead to larger polytopes. The corresponding polytope can be constructed with the working region in (λ_1, λ_2) plane and λ_3 varying range, and given by $A_1B_1D_1E_1A_3B_3D_3E_3$ and $A_1C_1D_1E_1A_2C_2D_2E_2$, respectively, in Fig. 10.

The proposed *double-buck-clamping* mode has the minimum polytope $D_1D_2E_2A_2$ and the optimal open-loop dynamics, in accordance with the analysis results.

D. Physical Explanation

The advantages of *double-buck-clamping* mode over the other *Transition* modes can also be physically explained. For the different *Transition* modes, an illustration of $v_o \sim d$ frequency response is shown in Fig. 11. The frequency response of *double-buck-clamping* mode fully locates within the frequency response range of *boost* mode. Therefore, when considering the total frequency response in *buck* mode, *boost* mode, and *Transition* mode, the *double-buck-clamping* mode will not increase the total frequency response range.

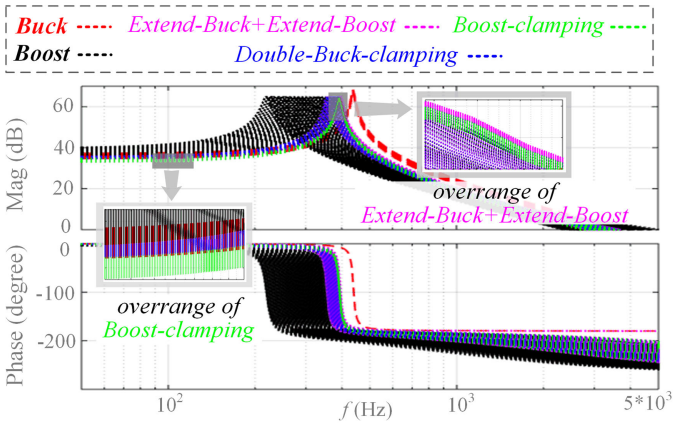

Fig. 11. Open-loop v_o~d frequency response of MBBC.

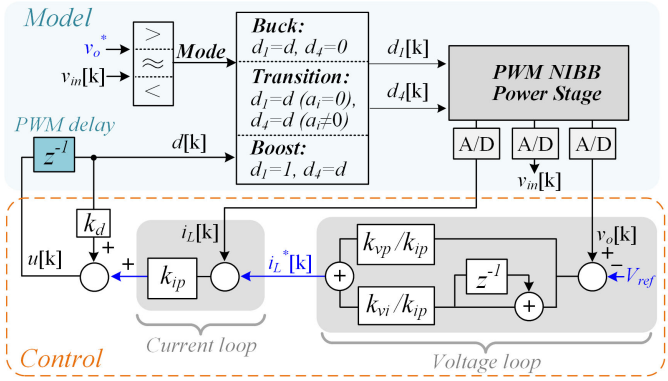

Fig. 12. Digital control diagram for multimode operation of MBBC.

In comparison, the frequency response band of *boost-clamping* mode and *extend-buck+extend-boost* mode overreaches the frequency response range of *buck* and *boost* mode. Therefore, the total frequency range becomes wider when adopting the above two types of *Transition* modes. It will results in more conservative control design. The strict mathematical reason can be explained with the LPV system discussed above.

Although the frequency response can provide a physical explanation, the conventional small-signal model would unable to deal with the multiple varying terms. Based on the LPV model, *double-buck-clamping* mode can be found, and this is one of the advantages for the proposed method.

IV. Close-Loop Control Design

Based on the LPV model, close-loop control design is analyzed in this section. To eliminate the steady-state v_o deviation, an additional variable $v_{\rm int}(k)$ is introduced as (17). The reference output voltage $V_{\rm ref}$ is taken as a constant value

$$v_{\rm int}\left(k+1\right)=v_{\rm int}\left(k\right)+\underbrace{\left[v_o\left(k\right)-V_{\rm ref}\right]}_{e(k)}. \tag{17}$$

Based on (17), the augmented state variable is given as $\boldsymbol{x}(k)$.

$$\tilde{\boldsymbol{x}}\left(k\right)=\left[\tilde{i}_L\left(k\right)\ \tilde{v}_o\left(k\right)\ \tilde{v}_{\rm int}\left(k\right)\ \tilde{d}\left(k\right)\right]^T. \tag{18}$$

The resulting discrete-time model is given as follows:

$$\tilde{x}\left(k+1\right)=\underbrace{\begin{bmatrix}1 & -\frac{T_s}{L}\lambda_1 & 0 & \frac{V_oT_s}{L}\lambda_3\\ \frac{T_s}{C}\lambda_1 & 1-\frac{T_s}{RC} & 0 & -\frac{I_{\rm load}T_s}{C}\lambda_2\\ 0 & 1 & 1 & 0\\ 0 & 0 & 0 & 0\end{bmatrix}}_{A(\lambda)}\tilde{x}\left(k\right)+\underbrace{\begin{bmatrix}0\\ -\frac{T_s}{C}\\ 0\\ 0\end{bmatrix}}_{B_w}\tilde{i}_s\left(k\right)+\underbrace{\begin{bmatrix}0\\ 0\\ 0\\ 1\end{bmatrix}}_{B_u}\tilde{u}\left(k\right) \tag{19}$$

$$\tilde{y}\left(k\right)=\underbrace{\begin{bmatrix}0&1&0&0\end{bmatrix}}_{C}\tilde{\boldsymbol{x}}\left(k\right). \tag{20}$$

For close-loop control, the widely applied linear control given by (21) is here adopted. The corresponding control diagram is shown in Fig. 12. The linear control can be restructured in classical dual-loop PI form. The differences are the elimination of integration at current loop and the consideration of one switching cycle control delay introduced by digital implementation.

$$\tilde{d}_{eq}\left(k\right)=\begin{bmatrix}k_{ip}&k_{vp}&k_{vi}&k_d\end{bmatrix}\tilde{\boldsymbol{x}}\left(k\right). \tag{21}$$

Robust stability and dynamic performance of the close-loop MBBC can be optimized with the following two linear matrix inequities, respectively.

Robust Stability: For optimization of load disturbance capability, the H_∞ norm $\|v_o\|_2/\|i_s\|_2$ is lower than μ, if there exist symmetric positive definite matrices w_i, w_j and matrices G, Z such that for $i=1,\ldots,N$, $j=1,\ldots,N$ (N refers to the number of vertexes of the polytopic working region)

$$\begin{bmatrix}G+G^T-w_i & * & * & *\\ \mathbf{0} & \mu\mathbf{I} & * & *\\ A_iG+B_uZ & B_w & w_j & *\\ C_iG & \mathbf{0} & \mathbf{0} & \mu\mathbf{I}\end{bmatrix}>0. \tag{22}$$

Dynamic Performance: For given real positive scalars r and d, defining the circle belonging to the unit circle as shown in Fig. 13. If there exist symmetric positive definite matrices w_i, w_j and matrices G, Z such that for $i=1,\ldots,N$, $j=1,\ldots,N$

$$\begin{bmatrix}G+G^T-w_i & *\\ r^{-1}\left(A_i-d\boldsymbol{I}\right)G+r^{-1}B_uZ & w_j\end{bmatrix}>0 \tag{23}$$

holds, then the close-loop eigenvalues are configured in the circular region shown in Fig. 13.

Based on (22) and (23), the control design can be easily implemented on MATLAB LMI toolbox. Proof of (22) can be found in [37]. Proof of (23) comes from *Theorem 4* [38] by replacing A_i and B with $r^{-1}(A_i-d\boldsymbol{I})$ and $r^{-1}B_u$, respectively. With the aid of LMI method, both robust stability and dynamic state performance can be guaranteed by fulfilling (22) and (23). The

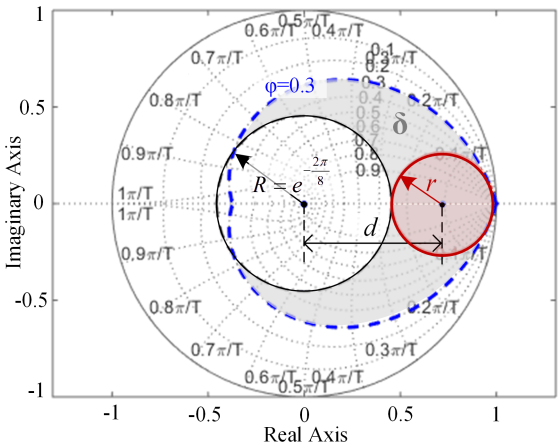

Fig. 13. Circular region (r, d) for close-loop eigenvalues of MBBC.

TABLE II
COMPARISON OF THE DESIGNED CONTROLLERS WITH DIFFERENT H_∞ NORMS AND DIFFERENT TRANSITION MODES

Transition mode	*Double-buck-clamping*	*Double-buck-clamping*	*Boost-clamping*	*Extend-buck+ extend-boost*
H_∞ norm μ	2.5	4	4	4
Dynamic parameters	d=0.727 r=0.272	d=0.719 r=0.264	d=0.719 r=0.274	d=0.719 r=0.272
Recovery time Δt (s)	0.15	0.008	0.02	0.16
Control parameters	k_{ip}=-0.023, k_{vp}=-0.008, k_{vi}=-2*10^{-6}, k_d=0.27	k_{ip}=-0.024, k_{vp}=-0.009, k_{vi}=-4.3*10^{-4}, k_d=0.26	k_{ip}=-0.02, k_{vp}=-0.006, k_{vi}=-1.7*10^{-4}, k_d=0.3	k_{ip}=-0.021, k_{vp}=-0.008, k_{vi}=-2.2*10^{-4}, k_d=0.27

feedback gain is given by

$$\left[k_{ip}\ k_{vp}\ k_{vi}\ k_d\right] = ZG^{-1}. \tag{24}$$

Under given load disturbance rejection capability indicated by the H_∞ norm μ, dynamic performance of MBBC can be optimized by adjusting the r and d values for close-loop eigenvalues. As shown in Fig. 13, to ensure damping ratio above $\varphi > 0.3$ and eigenvalues outside the circle $R = e^{-\frac{2\pi}{8}}$, the close-loop eigenvalues should confined within the region δ. This nonconvex region is approximated by a convex circular region with $d = 0.719$, $r = 0.264$. The recovery time Δt of close-loop converter is given by (25).

$$\Delta t < -\frac{3}{f_s \ln(d+r)}. \tag{25}$$

For eigenvalue region $d = 0.719$, $r = 0.264$, the corresponding H_∞ norm is given by 4 (12 dB) and the control gains are listed in Table II. According to (25), the close-loop recovery time is below 10 ms. Note that dynamic response and disturbance rejection are two often contradictory design objectives. The H_∞ norm can be decreased to 2.5 with eigenvalue region $d = 0.727$, $r = 0.272$. As a result, the recovery time would increase up to 0.15 s. For a balance between dynamic response and disturbance rejection, here the H_∞ norm is selected at 4.

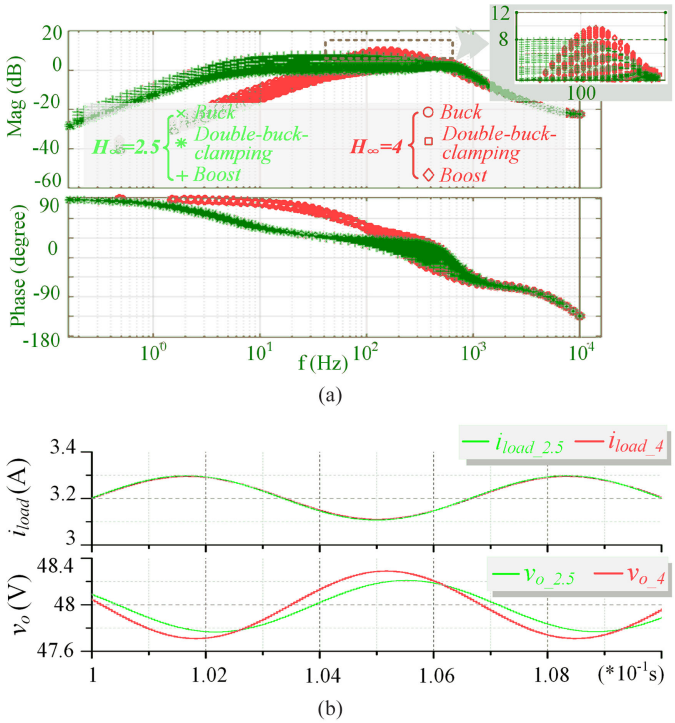

Fig. 14. Illustration of load disturbance rejection capability in frequency domain and time domain (with different designed H_∞ norm of 2.5 and 4). (a) Comparison of $v_o \sim i_s$ frequency response. (b) Comparison of v_o under load disturbance.

To evaluate the influence of different *Transition* modes, the control gains are also synthesized with *boost-clamping* mode and *extend-buck+extend-boost* mode. For fair comparison, the center of the circle (d) remains constant and the radius r is increased to attain the same H_∞ norm value of 4. With the increase of r, the close-loop eigenvalues are approaching the unit circle, indicating longer recovery time. The developed control parameters and the related r values are compared in Table II.

With the control gains in Table II, an illustration of the load disturbance rejection capability is shown in Fig. 14. Take *double-buck-clamping* mode as an example, with different μ designs, the measured close-loop $v_o \sim i_s$ frequency responses are compared in Fig. 14(a). The magnitude are constrained below 2.5 (8 dB) and 4 (12 dB), respectively, in accordance with the disturbance rejection design goals. In time domain, a 150 Hz disturbance is imposed at current source load i_s. The corresponding output voltage $v_{o\_2.5}(t)$ and $v_{o\_4}(t)$ are compared in Fig. 14(b). A marginal improvement of output voltage can be observed in $v_{o\_2.5}(t)$, in accordance with the analysis results.

However, this marginal improvement of load disturbance rejection capability comes at a significant degradation of dynamic performance, as shown in the following.

A comparison of the close-loop MBBC eigenvalues under varying load R and input voltage v_{in} is illustrated in Fig. 15. For different *Transition* modes and different H_∞ norms, the close-loop eigenvalues are all within the corresponding circles, in verification of the LMI design method. Besides, compared with the design case of $\mu = 4$, the close-loop eigenvalues with

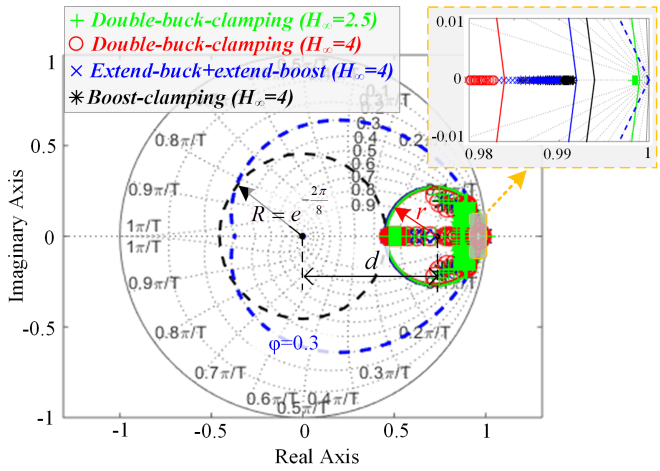

Fig. 15. Comparison of close-loop eigenvalues with the developed control parameters in Table II.

$\mu = 2.5$ are very near the unit circle as shown in Fig. 15 and the recovery time reaches 0.15 s. For a balance between robust stability and dynamic response, the H_∞ norm μ is selected at 4.

Following conditions should be noted:

1) In open-loop analysis, although both two cases of $V_o/V_{\min} \geq 1/D_{\max}{}^2$ and $V_o/V_{\min} < 1/D_{\max}{}^2$ are discussed, the majority of practical applications belongs to the first scenario. For maximum duty ratio $D_{\max} > 0.9$, it requires $V_o/V_{\min} > 1.2$. This requirement is well met in typical applications of MBBC as in [6]–[16], and *double-buck-clamping* mode obtains the minimum polytopic working region.
2) In close-loop control design, load disturbance rejection capability and fast dynamic response are two often contradictory goals. In the proposed algorithm, the dynamic response is optimized under the constraint of preset load disturbance capability indicated by H_∞ norm.

V. Experimental Verifications

In verification of the optimization algorithm, a prototype of MBBC has been built. Specifications of the circuit parameters follow Table I. The linear digital control is implemented on TI TMS320C6657, and the sampling rate is the same as switching frequency $f_s = 20$ kHz. The current source load is implemented on an electronic load (Chroma 63600). The designed controllers are tested for robust voltage regulation, comparatively evaluated with small-signal PI controller, and comparatively evaluated of different *Transition* modes.

A. Stability Under Multimode Operation

For the different *Transition* modes, the designed controllers are tested with varying input voltage v_{in}. As is shown in Fig. 16(a)–(c), when the input voltage v_{in} increases from 24 to 72 V at a slope of 20 V/s, MBBC working mode autonomously changes from *boost* mode to the selected *Transition* mode and to *buck* mode.

Compared with *extend-buck+extend-boost* mode, the *double-buck-clamping* mode has higher inductor current. For typical $D_{\max} = 0.9$, the inductor current of *double-buck-clamping* mode can reach at most 1.11 times *extend-buck+extend-boost* mode. Both the two *Transition* modes have lower inductor current compared with *boost-clamping* mode. For all three *Transition* modes, the designed controllers can ensure robust voltage regulation through the wide operation range, in accordance with the analysis results.

Besides, voltage overshoot appears during mode transition. In comparison, the *double-buck-clamping* mode has the lowest voltage overshoot, followed by *extend-buck+extend-boost* mode. The *boost-clamping* mode has the largest voltage overshoot. The results further support the analysis result that *double-buck-clamping* mode has the fastest dynamic response

B. Comparison With PI Control

A comparison of the small-signal model based PI control and the proposed control is shown in Fig. 17. Here, the *Transition* mode is selected as *boost-clamping* mode. For small-signal model based PI control, the control parameters follow Section II-B. For LPV control, to attain recovery time below 5 ms and damping ratio below 0.3, r is selected as 0.382 and d is selected as 0.59. As shown in Fig. 17(a), under the same load disturbance, the LPV-based control has near the same voltage deviation as small-signal PI control in *buck* mode. However, in Fig. 17(b), the small-signal PI control has lower damping ratio and longer recovery time in *Transition* mode. In *boost* mode of Fig. 17(c), the damping ratio of small-signal PI control becomes even lower, and results in larger voltage overshoot.

In comparison, small-signal PI control can only provide performance optimization at the selected working mode (i.e., *buck* mode) and steady-state point. For the other working modes, the dynamic response would deteriorate. LPV-based control can guarantee dynamic performance considering the multiple modes and wide working range, in accordance with the analysis results.

C. Comparison of Dynamic Responses With Different Transition Mode

In verification of the proposed *double-buck-clamping* transition mode, the designed control parameters in Table II are compared under load disturbance.

In *boost* mode, the input voltage v_{in} is set as 35 V and the voltage deviation and recovery time are measured with current source load increases from 0 to 4 A. As shown in Fig. 18(a), under different *Transition* modes, the corresponding recovery time Δt and voltage deviation Δv are as follows.

1) *Double-buck-clamping mode:* $\Delta t = 6$ ms, $\Delta v = 5.8$ V.
2) *Extend-buck+extend-boost mode:* $\Delta t = 12$ ms, $\Delta v = 5.8$ V.
3) *Boost-clamping mode:* $\Delta t = 15$ ms, $\Delta v = 6$V.

In *Transition* mode, the input voltage v_{in} is set as 45 V and the voltage deviation and recovery time are measured with current source load increases from 0 to 4 A. As shown in Fig. 18(b),

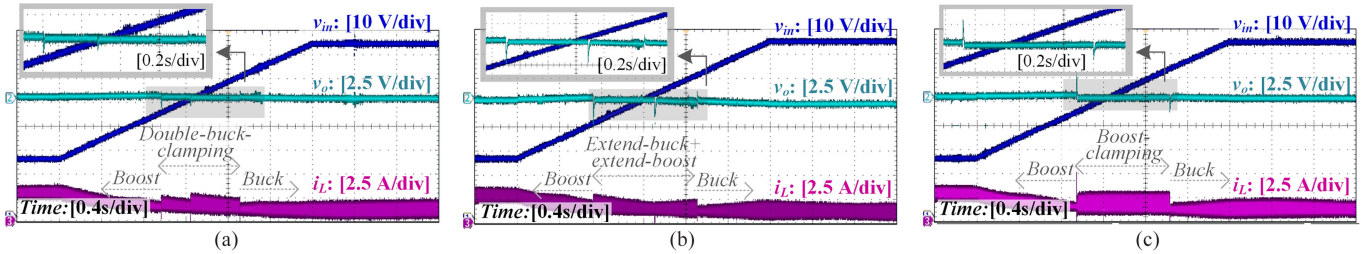

Fig. 16. Robust voltage regulation of MBBC through wide operation range. (a) *Transition* mode: *Double-buck-clamping mode*. (b) *Transition* mode: *Extend-buck+extend-boost mode*. (c) *Transition* mode: *Boost-clamping mode*.

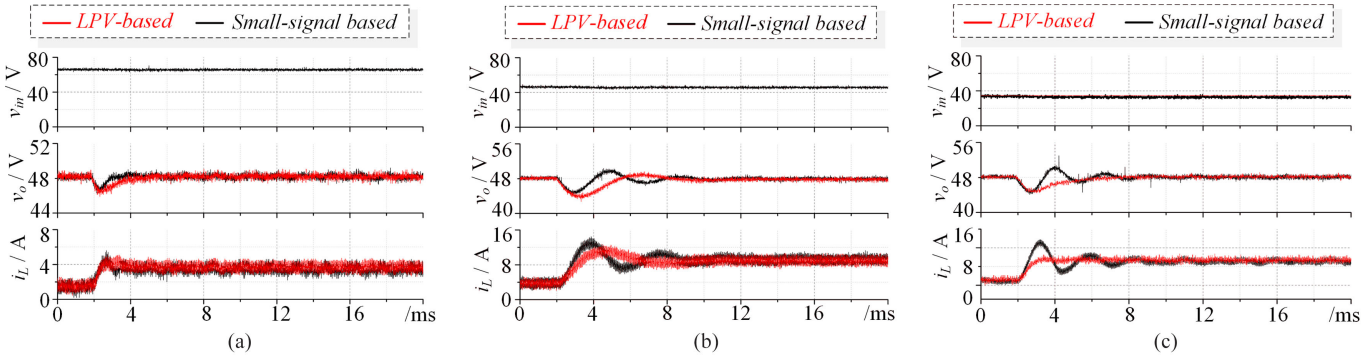

Fig. 17. Comparison of LPV-based control with small-signal PI control. (a) *Buck* mode, $v_{\rm in} = 65$ V. (b) *Transition* mode, $v_{\rm in} = 45$ V. (c) *Boost* mode, $v_{\rm in} = 35$ V.

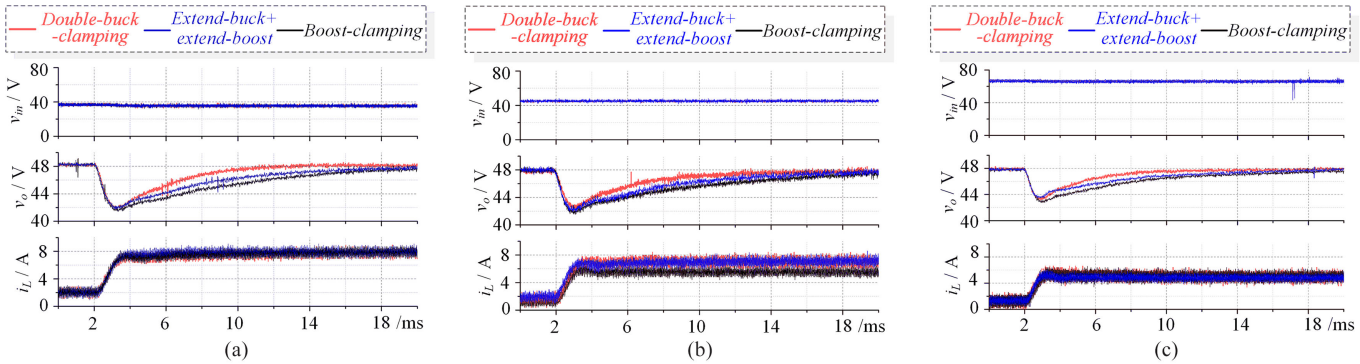

Fig. 18. Comparison of MBBC dynamic response with different *Transition* modes. (a) *Boost* mode. (b) *Transition* mode. (c) *Buck* mode.

under different *Transition* modes, the corresponding recovery time Δt and voltage deviation Δv are as follows.

1) *Double-buck-clamping mode:* $\Delta t = 7$ ms, $\Delta v = 5.5$ V.
2) *Extend-buck+extend-boost mode:* $\Delta t = 11$ ms, $\Delta v = 5.5$ V.
3) *Boost-clamping mode:* $\Delta t = 13$ ms, $\Delta v = 6$ V.

In *buck* mode, the input voltage $v_{\rm in}$ is set as 65 V and the voltage deviation and recovery time are measured with current source load increases from 0 to 4 A. As shown in Fig. 18(c), with different *Transition* modes, the corresponding recovery time Δt and voltage deviation Δv are as follows.

1) *Double-buck-clamping mode:* $\Delta t = 7$ ms, $\Delta v = 5$ V.
2) *Extend-buck+extend-boost mode:* $\Delta t = 11$ ms, $\Delta v = 5$ V.
3) *Boost-clamping mode:* $\Delta t = 13$ ms, $\Delta v = 5.4$ V.

In comparison, *double-buck-clamping* mode has the minimum recovery time and voltage deviation. The experimental results are in well agreement with the analysis results in Section III.

VI. Conclusion

MBBC exhibits different dynamic properties under different working modes. Potential instability and design challenge of small-signal model based control is first analyzed. To account for the dynamic difference, the converter has been modeled as an LPV system. Both open-loop *Transition* mode and close-loop linear control gains has been collaboratively optimized for fast and robust voltage regulation. Key findings of this article are as follows:

1) Size of operation region serves as an effective criterion for evaluation of the dynamic influence of different *Transition* modes.
2) A novel *Transition* mode "*Double-buck-clamping*" has been proposed for the optimal open-loop dynamic performance.
3) Based on the operation region, a linear control design algorithm has been proposed for optimization of recovery time and damping ratio with guaranteed robust stability.

The developed linear control gains have been tested through wide operation range in verification of robust stability. The proposed "*double-buck-clamping*" mode has been compared with existing "*boost-clamping*" mode, "*extend-buck+extend-boost*" and shows the fastest load response.

As a fundamental type of multimode converter, the LPV modeling and analysis approach of MBBC can also be applied for other multimode power converters.

REFERENCES

[1] R. S. Waffler and J. W. Kolar, "A novel low-loss modulation strategy for high-power bidirectional buck+boost converters," *IEEE Trans. Power Electron.*, vol. 24, no. 6, pp. 1589–1599, Jun. 2009.

[2] M. Anun, M. Ordonez, I. G. Zurbriggen, and G. G. Oggier, "Circular switching surface technique: High-performance constant power load stabilization for electric vehicle systems," *IEEE Trans. Power Electron.*, vol. 30, no. 8, pp. 4560–4572, Aug. 2015.

[3] M. Rodriguez, G. Stahl, L. Corradini, and D. Maksimovic, "Smart DC power management system based on software-configurable power modules," *IEEE Trans. Power Electron.*, vol. 28, no. 4, pp. 1571–1586, Apr. 2013.

[4] J. M. Guerrero, P. C. Loh, T. Lee, and M. Chandorkar, "Advanced control architectures for intelligent microgrids—Part II: Power quality, energy storage, and AC/DC microgrids," *IEEE Trans. Ind. Electron.*, vol. 60, no. 4, pp. 1263–1270, Apr. 2013.

[5] T. Suntio, T. Messo, and J. Puukko, *Power Electronic Converters: Dynamics and Control in Conventional and Renewable Energy Applications*. Weinheim, Germany: Wiley-VCH, 2017.

[6] F. Akar, Y. Tavlasoglu, E. Ugur, B. Vural, and I. Aksoy, "A bidirectional nonisolated multi-input DC–DC converter for hybrid energy storage systems in electric vehicles," *IEEE Trans. Veh. Technol.*, vol. 65, no. 10, pp. 7944–7955, Oct. 2016.

[7] I. Aharon, D. Shmilovitz, and A. Kuperman. "Multimode power processing interface for fuel cell range extender in battery powered vehicle," *Appl. Energy*, vol. 204, pp. 572–581, 2017.

[8] D. Zhou, J. Wang, N. Hou, Y. Li, and J. Zou, "Dual-port inverters with internal DC-DC conversion for adjustable DC-link voltage operation of electric vehicles," *IEEE Trans. Power Electron.*, to be published.

[9] J. Wang, K. Sun, H. Wu, J. Zhu, Y. Xing, and Y. Li, "Hybrid connected unified power quality conditioner integrating distributed generation with reduced power capacity and enhanced conversion efficiency," *IEEE Trans. Ind. Electron.*, to be published.

[10] J. Chen, P. Shen, and Y. Hwang, "A high-efficiency positive buck–boost converter with mode-select circuit and feed-forward techniques," *IEEE Trans. Power Electron.*, vol. 28, no. 9, pp. 4240–4247, Sep. 2013.

[11] P. Huang, W. Wu, H. Ho, and K. Chen, "Hybrid buck–boost feedforward and reduced average inductor current techniques in fast line transient and high-efficiency buck–boost converter," *IEEE Trans. Power Electron.*, vol. 25, no. 3, pp. 719–730, Mar. 2010.

[12] D. Kim and B. Lee, "An enhanced control algorithm for improving the light-load efficiency of noninverting synchronous buck–boost converters," *IEEE Trans. Power Electron.*, vol. 31, no. 5, pp. 3395–3399, May 2016.

[13] C. W. Chen, K. H. Chen, and Y. M. Chen, "Modeling and controller design of an autonomous PV module for DMPPT PV systems," *IEEE Trans. Power Electron.*, vol. 29, no. 9, pp. 4723–4732, Sep. 2014.

[14] L. Callegaro, M. Ciobotaru, D. J. Pagano, and J. E. Fletcher, "Feedback linearization control in photovoltaic module integrated converters," *IEEE Trans. Power Electron.*, vol. 34, no. 7, pp. 6876–6889, Jul. 2019.

[15] Y. Lee, A. Khaligh, A. Chakraborty, and A. Emadi, "Digital combination of buck and boost converters to control a positive buck–boost converter and improve the output transients," *IEEE Trans. Power Electron.*, vol. 24, no. 5, pp. 1267–1279, May 2009.

[16] Y. Y. Tsai, Y. S. Tsai, C. W. Tsai, and C. H. Tsai, "Digital noninverting buck-boost converter with enhanced duty-cycle-overlap control," *IEEE Trans. Circuits Syst. II: Exp. Briefs*, vol. 64, no. 1, pp. 41–45, Jan. 2017.

[17] Y. Lee, A. Khaligh, and A. Emadi, "A compensation technique for smooth transitions in a noninverting buck–boost converter," *IEEE Trans. Power Electron.*, vol. 24, no. 4, pp. 1002–1015, Apr. 2009.

[18] D. C. Jones and R. W. Erickson, "Buck-boost converter efficiency maximization via a nonlinear digital control mapping for adaptive effective switching frequency," *IEEE J. Emerg. Sel. Topics Power Electron.*, vol. 1, no. 3, pp. 153–165, Sep. 2013.

[19] C. Restrepo, T. Konjedic, J. Calvente, and R. Giral, "Hysteretic transition method for avoiding the dead-zone effect and subharmonics in a noninverting buck–boost converter," *IEEE Trans. Power Electron.*, vol. 30, no. 6, pp. 3418–3430, Jun. 2015.

[20] L. Callegaro, M. Ciobotaru, D. J. Pagano, E. Turano, and J. E. Fletcher, "A simple smooth transition technique for the noninverting buck–boost converter," *IEEE Trans. Power Electron.*, vol. 33, no. 6, pp. 4906–4915, Jun. 2018.

[21] N. Zhang, G. Zhang, and K. W. See, "Systematic derivation of dead-zone elimination strategies for the noninverting synchronous buck–boost converter," *IEEE Trans. Power Electron.*, vol. 33, no. 4, pp. 3497–3508, Apr. 2018.

[22] Z. Zhao, M. Xu, Q. Chen, J. Lai, and Y. Cho, "Derivation, analysis, and implementation of a boost–buck converter-based high-efficiency PV inverter," *IEEE Trans. Power Electron.*, vol. 27, no. 3, pp. 1304–1313, Mar. 2012.

[23] C. Yao, X. Ruan, W. Cao, and P. Chen, "A two-mode control scheme with input voltage feed-forward for the two-switch buck-boost DC–DC converter," *IEEE Trans. Power Electron.*, vol. 29, no. 4, pp. 2037–2048, Apr. 2014.

[24] R. Paul, L. Sankey, L. Corradini, Z. Popovic, and D. Maksimovic, "Power management of wideband code division multiple access RF power amplifiers with antenna mismatch," *IEEE Trans. Power Electron.*, vol. 25, no. 4, pp. 981–991, Apr. 2010.

[25] J. Ma, M. Zhu, X. Li, and X. Cai, "Bumpless transfer of non-inverting buck boost converter among multiple working modes," in *Proc. IEEE Appl. Power Electron. Conf. Expo.*, 2018, pp. 1909–1914.

[26] C. L. Wei, C. H. Chen, K. C. Wu, and I. T. Ko, "Design of an average-current-mode noninverting buck–boost DC–DC converter with reduced switching and conduction losses," *IEEE Trans. Power Electron.*, vol. 27, no. 12, pp. 4934–4943, Dec. 2012.

[27] J. Ma, M. Zhu, G. He, and X. Cai, "Breaking performance limit of asynchronous control for non-inverting buck boost converter," in *Proc. 43rd Annu. Conf. IEEE Ind. Electron. Soc.*, 2017, pp. 928–933.

[28] M. Agostinelli, S. Fabbro, R. Priewasser, S. Marsili, and M. Huemer, "Pseudo sliding mode control for a positive Buck-Boost converter IC in 0.13 µm CMOS," in *Proc. 28th Annu. IEEE Appl. Power Electron. Conf. Expo.*, 2013, pp. 2551–2554.

[29] M. E. Şahın, H. İ. Okumuş, and H. Kahvecı, "Sliding mode control of PV powered DC/DC buck-boost converter with digital signal processor," in *Proc. 17th Eur. Conf. Power Electron. Appl.*, 2015, pp. 1–8.

[30] G. A. Ramos, R. A. Soto-Perez, and J. A. Cifuentes, "A varying frequency LPV-based control strategy for three-phase inverters," *IEEE Trans. Ind. Electron.*, vol. 64, no. 9, pp. 7599–7608, Sep. 2017.

[31] C. Olalla, R. Leyva, I. Queinnec, and D. Maksimovic, "Robust gain-scheduled control of switched-mode DC–DC converters," *IEEE Trans. Power Electron.*, vol. 27, no. 6, pp. 3006–3019, Jun. 2012.

[32] L. Corradini, D. Maksimovic, P. Mattavelli, and R. Zane, *Digital Control of High-Frequency Switched-Mode Power Converters*, 1st ed. New York, NY, USA: Wiley, 2015.

[33] B. Stephen, and L. Vandenberghe, *Convex Optimization*. Cambridge, U.K.: Cambridge Univ. Press, 2004.

[34] A. P. White, G. Zhu, and J. Choi, *Linear Parameter-Varying Control for Engineering Applications*. Berlin, Germany: Springer, 2013.

[35] Min Chen and G. A. Rincon-Mora, "Accurate electrical battery model capable of predicting runtime and I-V performance," *IEEE Trans. Energy Convers.*, vol. 21, no. 2, pp. 504–511, Jun. 2006.

[36] E. Barsoukov and J. R. Macdonald, *Impedance Spectroscopy: Theory, Experiment, and Applications*, 2nd ed. New York, NY, USA: Wiley, 2005.

[37] L. A. Maccari *et al.*, "Robust H_∞ control for grid connected PWM inverters with LCL filters," in *Proc. 10th IEEE/IAS Int. Conf. Ind. Appl.*, 2012, pp. 1–6.
[38] J. Daafouz and J. Bernussou, "Parameter dependent Lyapunov functions for discrete time systems with time varying parametric uncertainties," *Syst. Control Lett.*, vol. 43, no. 5, pp. 355–359, 2001.

Jianjun Ma (Member, IEEE) received the B.S. degree from Xi'an Jiaotong University, Xi'an, China, in 2013, and the Ph.D. degree from Shanghai Jiao Tong University, Shanghai, China, in 2019, both in electrical engineering.

Since January 2020, he has been a Postdoctoral Research Fellow with the Department of Electrical Engineering, Shanghai Jiao Tong University, Shanghai, China. His research interests include renewable energy integration, dc distributed power system, and dc grid.

Miao Zhu (Senior Member, IEEE) received the B.Sc. degree from Southeast University, Nanjing, China, in 2001, and the Ph.D. degree from Nanyang Technological University, Singapore, in 2009, both in electrical engineering.

From 2001 to 2002, he was an Assistant Engineer with Wuxi Power Supply Company, State Grid of China. From 2008 to 2009, he was with Meiden Asia Pte Ltd, Singapore, as an R&D Engineer. After that, he had been a Scientist with the Experimental Power Grid Centre, A∗STAR, Singapore. In August 2012, he joined as a Research Professor with the honor title of Distinguished Researcher with Shanghai Jiao Tong University (SJTU), Shanghai, China, where he is currently a Professor with the Electrical Engineering Department. He is also the the Vice Director with the State Energy Smart Grid (Shanghai) R&D Centre He is a regular reviewer for a number of academic journals, and has authored/coauthored nearly 90 papers in refereed journals and conferences proceedings. His research interests include power converters, renewable energy generation, dc distributed power system, and dc grid.

Prof. Zhu is the recipient of 2009 IEEE Power Electronics Society Prize Letter Award. In 2010, he was awarded the World Future Foundation PhD Prize in Environmental and Sustainability Research. In 2018, he was appointed as the PI/Chief Scientist of the National Key R&D Program of China under 2018YFB0904100. He has been the Vice Chairman of both IEEE PELS Shanghai Chapter and IEEE IES Shanghai Chapter since 2018.

Yunwei Li (Fellow, IEEE) received the B.Sc. degree in electrical engineering from Tianjin University, Tianjin, China, in 2002, and the Ph.D. degree from Nanyang Technological University, Singapore, in 2006.

In 2005, he was a Visiting Scholar with Aalborg University, Aalborg, Denmark. From 2006 to 2007, he was a Postdoctoral Research Fellow with Ryerson University, Toronto, ON, Canada. In 2007, he also worked with Rockwell Automation Canada. He then joined the University of Alberta, Edmonton, AB, Canada, where he is currently a Professor. His research interests include distributed generation, microgrid, renewable energy, high power converters, and electric motor drives.

Dr. Li serves as an Editor-in-Chief for the IEEE TRANSACTIONS ON POWER ELECTRONICS LETTERS. Prior to that, he was Associate Editor for the IEEE TRANSACTIONS ON POWER ELECTRONICS, the IEEE TRANSACTIONS ON INDUSTRIAL ELECTRONICS, the IEEE TRANSACTIONS ON SMART GRID, and the IEEE JOURNAL OF EMERGING AND SELECTED TOPICS IN POWER ELECTRONICS. He was the recipient of the Richard M. Bass Outstanding Young Power Electronics Engineer Award from IEEE POWER ELECTRONICS SOCIETY in 2013 and the Second Prize Paper Award of IEEE TRANSACTIONS ON POWER ELECTRONICS in 2014. He is listed as a Highly Cited Researcher by the Web of Science Group.

Xu Cai received the B.Eng. degree from Southeast University, Nanjing, China, in 1983, the M.Eng. and Ph.D. degrees from China University of Mining and Technology, Jiangsu, China, in 1988 and 2000, respectively, all in electrical engineering.

He was with the Department of Electrical Engineering, China University of Mining and Technology, as an Associate Professor, from 1989 to 2001. He was the Vice Director with the State Energy Smart Grid R&D Center, Shanghai, China, from 2010 to 2013. Since 2002, he has been a Professor with Shanghai Jiao Tong University, Shanghai, where he has also been the Director of the Wind Power Research Center, since 2008. His research interests include power electronics and renewable energy exploitation and utilization, including wind power converters, wind turbine control system, large power battery storage systems, clustering of wind farms and its control system, and grid integration.